Effects of aging processes at the surface of the superconductor β-FeSe

L. Lanoël,[1,*] G. Rozas,[1] A. E. Bruchhausen,[1] M. L. Amigó,[1] M. V. Ale Crivillero,[2] J. A. Hofer,[1] M. Villafuerte,[3] G. Bridoux,[3] S. Bengió,[1] and G. Nieva[1,†]

[1]*Centro Atómico Bariloche-CNEA, Instituto Balseiro - UNCuyo, Instituto de Nanociencia y Nanotecnología, CNEA, CONICET, Avda. E. Bustillo 9500, R8402AGP S.C. de Bariloche, Río Negro, Argentina*

[2]*Max Planck Institute for Chemical Physics of Solids, Nöthnitzer Strasse 40, 01187 Dresden, Germany*

[3]*Laboratorio de Física del Sólido (CONICET-UNT) INFINOA-Facultad de Ciencias Exactas y Tecnología, Universidad Nacional de Tucumán, Av. Independencia 1800, San Miguel de Tucumán, Argentina*

(Received 18 September 2021; revised 17 November 2022; accepted 22 November 2022; published 8 December 2022)

This work reports a complete analysis of surface degradation in β-FeSe single crystals; which includes the dependence on aging and temperature of Raman spectra, electrical transport resistivity, and XPS depth profiling characterization. All measurements are consistent with the emergence of clusters of Se and the presence of FeO_x in the surface of the crystals. The vibrational modes of the Se clusters are coupled to the β-FeSe ones as seen in the structural transition. Moreover, this degraded surface can behave like a quasi-two-dimensional layer, as supported by a theoretical model and also consistent with Raman spectra. While the degradation of thin films of β-FeSe in air is widely known, with a corresponding loss of the superconducting properties, in single crystals with aged surfaces we observe an enhancement of the superconducting properties.

DOI: 10.1103/PhysRevB.106.214507

I. INTRODUCTION

Iron selenide (β-FeSe) is a superconductor with tetragonal crystal structure at room temperature, which becomes orthorhombic when cooled below the nematic transition temperature around 90 K. It has a superconducting critical temperature $T_c = 8$ K that goes up to 37 K [1] when a pressure of 9 GPa is applied along the c axis. β-FeSe presents no magnetic order down to its superconducting transition temperature [2], which may suggest a strong relationship between the appearance of superconductivity and the normal vibrational modes of the crystal [3]. Selenium atoms and iron atoms vibrational modes A_{1g} and B_{1g}, respectively [4], are the only Raman active modes in the c-axis backscattering geometry, according to the space group $P4/nmm$ of the system.

This material is composed of stacked Fe-Se sheets bonded by van der Waals forces along the c axis [5,6]. This makes the crystal very easy to cleave, exposing a clean fresh surface. In addition, similar to what occurs for other selenides, the surface of β-FeSe draws great interest related to the potential experimental manifestation of Dirac-like states [7–9]. This fact and the search of topologically protected states in other selenides (e.g., Bi_2Se_3) or novel sensing devices (e.g., $MoSe_2$, $TiSe_2$, $TaSe_2$) has promoted the analysis of surface vibrational states in Raman experiments. In several of these systems, as in β-FeSe, extra peaks appear in very thin samples. The ubiquity of a peak around 250 cm^{-1} in several systems as Bi_2Se_3 [10–12] $MoSe_2$ [13], $TiSe_2$ [14,15], and $TaSe_2$ [16], is a challenge since varied interpretations have been proposed in the literature for this feature.

Amorphous selenium is commonly used to create a protective layer to reduce reactivity of the surfaces and enhance rigidity. This selenium surface capping treatment is used to allow *ex situ* measurements out of the growth chambers or furnace capsules, since a thermal decapping at low temperatures ($\sim$200 °C) is possible [17].

In the present work, when Raman spectra are collected on a recently cleaved surface, we distinguish two peaks, attributed to A_{1g}(Se) and B_{1g}(Fe). As time passes, another peak at 250 cm^{-1} progressively appears.

An associated effect is also revealed in the superconducting properties since we observe an enhancement of the superconducting transition temperature in the aged samples. This effect is also observed in β-FeSe by reducing the thickness [18].

In order to elucidate the surface phenomena evolution, we performed temperature (5–800 K) and polarization dependent Raman spectra measurements. We also studied the surface chemical composition through x-ray photoelectron spectroscopy (XPS) on fresh and aged samples as a function of depth. The results unveil the presence of iron oxide in the aged samples, which results in material segregation. The aged surface is composed of a mixture of FeO_x, bonded Se ions, FeSe in ionic bonding, and β-FeSe. Furthermore, we calculated the dispersion relationship in the harmonic approximation for a *single* sheet of β-FeSe. These calculations predict three Raman active optical phonon modes near the center of the Brillouin zone: one attributed to Se vibrations, another to Fe vibrations, and the last one to a combination of vibrations of both kinds of atoms. This calculated last mode is curiously coincident with the main peak appearing with aging in our samples, attributed to amorphous selenium [19,20].

*lucio.lanoel@ib.edu.ar
†gnieva@cab.cnea.gov.ar

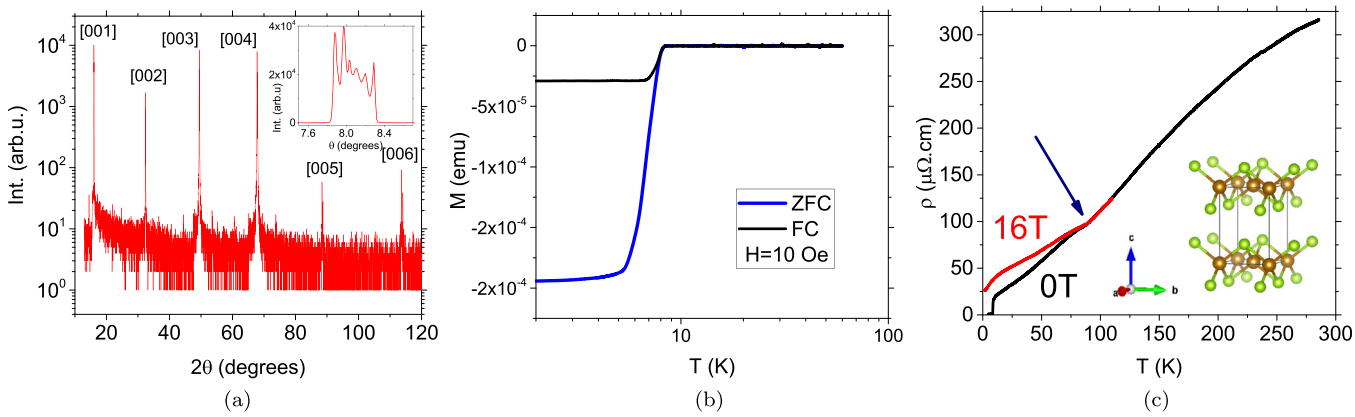

FIG. 1. (a) X-ray θ-2θ diffractogram showing only 00l reflexions. Inset: The rocking curve around the [001] peak is shown. (b) Magnetization ZFC-FC (cooling in zero field and in an applied field of 10 Oe). (c) Electrical resistivity vs temperature curves with 16 T and with no applied field. The arrow points out the nematic transition temperature. In the inset a unit cell of β-FeSe is shown. Green corresponds to Se and brown to Fe.

II. EXPERIMENTAL DETAILS

Samples were grown using the flux method in a mixture of KCl and $AlCl_3$ salts, for more than a month in an evacuated SiO_2 ampoule at 395 °C [21]. Further details on the crystal growth method can be found in Ref. [3].

The crystals were fixed to a holder inside a cryostat and a furnace, using GE7031 resin and silver paste, respectively, where micro-Raman spectra were collected in backscattering geometry over a wide range of temperature (5–800 K). For these measurements we employed a Horiba Scientific LabRAM HR Evolution spectrometer equipped with ×10, ×20, and ×100 objectives. Excitation was done using a 633 nm He-Ne laser.

The surface chemical composition and chemical state of the samples were studied by x-ray photoelectron spectroscopy (XPS) using a monochromatic Al K_α x-ray source (1486.71 eV) and a 150 mm hemispherical spectrometer (*Phoibos150, SPECS*). For the analysis, the samples were mounted on adhesive graphitic carbon tape. The binding energy (BE) scale was determined by measuring the Fermi level cutoff and the *C*1*s* from the tape (284.5 eV).

The topology of the samples was characterized by atomic force microscopy (AFM) measurements in a Dimension 3100 Brucker microscope. The AFM image was performed in tapping mode. For the stoichiometry and morphology characterization we use a FEI Quanta200 scanning electron microscope (SEM). X-ray spectra were taken in a PANalytical Empyrean diffractometer. Magnetization measurements were performed in a MPMS-5S QD-SQUID magnetometer. We carried out resistivity measurements in a standard cryostat, using a four contact configuration.

III. RESULTS

A. General sample characterization

In Fig. 1 we show a x-ray diffractogram, magnetization vs temperature (T) and electrical resistivity vs T characterization measurements, displaying typical β-FeSe features [22]. The electrical transport curve has a typical shape from 300 to 2 K with its characteristic kink around ≈90 K [indicated by the arrow in Fig. 1(c)], positive magnetoresistance (when the field is applied parallel to the c axis) below the nematic transition temperature, and a $T_c = 8.4$ K. Magnetization measurements confirm no magnetic order down to the superconducting transition temperature and x-ray diffraction confirms the β-FeSe phase with no evidence of spurious phases. When the samples are fresh out of the furnace they exhibit a gray metallic, homogeneous surface. In Fig. 2(a) a photograph of the sample in the Raman spectrometer is shown, the pale pink color is due to reflections from the incident source. The lumps observed in AFM images [Figs. 2(c) and 2(d)] are the first indication of the surface degradation [23]. They tend to grow in diameter and height as the sample ages. As this happens, the color of the surface changes. In Fig. 2(b) a partially cleaved sample is shown. The surface steps heights between aged and cleaved part, measured by AFM, result in a mean value of ≈86 nm, which is an upper bound of the thickness of the aged surface.

Raman measurements on samples fresh out of the furnace or freshly cleaved show two peaks as seen in Fig. 3, in good

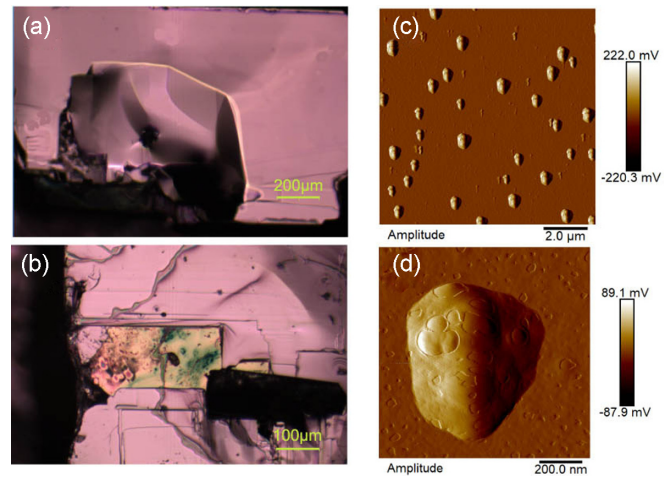

FIG. 2. (a) Photo of a sample immediately after taken out of the furnace. (b) Photo of an aged sample where part of the surface was cleaved (homogeneous pale pink part) and some part was not (yellow-green color part). (c) AFM deflection image of the cleaved zone some days after being made, where multiple clusters with the same shape can be seen. (d) Zoom on one cluster from image (c).

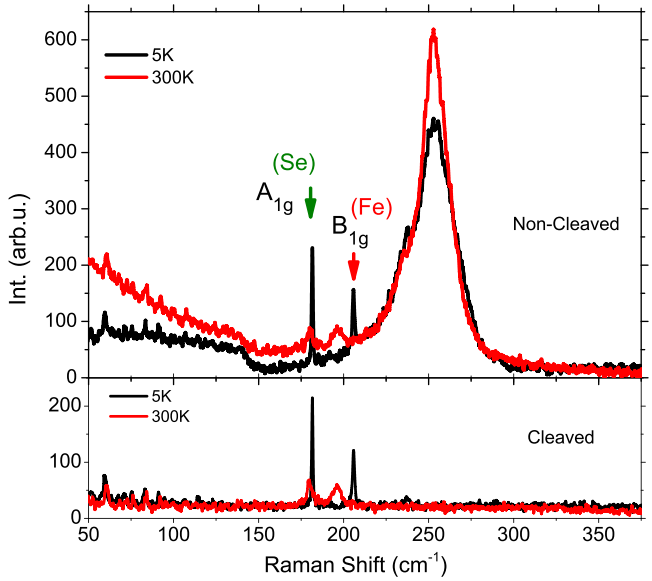

FIG. 3. Raman measurements of the cleaved and noncleaved samples (bottom and top panels) at 300 (red line) and 5 K (black line). Both measurements were made in parallel polarization configuration. The arrows indicate the bulk Se and Fe vibrational modes.

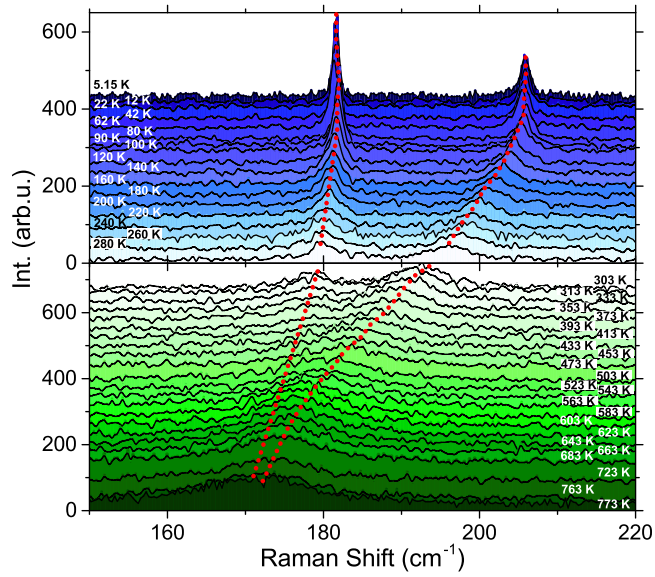

FIG. 4. Raman measurements of the cleaved part of the sample as a function of temperature. Upper section shows measurements below room temperature and lower section measurements above room temperature. The spectra spacing is proportional to the temperature difference between them. The red dotted line indicates the peak positions as a guide to the eye. See more detailed analysis in Fig. 7.

agreement with the one reported in Ref. [24]. After aging at room temperature in air for tens of days, a new broad peak appears at 250 cm^{-1}, with a low energy shoulder around 233 cm^{-1}. Another observed feature is the appearance of a low energy broad phonon tail below 150 cm^{-1} as can be seen in Fig. 3. This feature may correspond to the presence of amorphous Se as we will discuss later. Fresh samples only show a flat, low intensity background below this energy, with no temperature dependence, as can be seen in the lower panel of Fig. 3 for comparison. The use of different spot sizes [different objectives 10× (NA 0.20) to 100× (NA 0.90)] has no effect on the resulting spectra.

Measurements in air increasing the incident laser power on an aged sample (not shown) show that all the peaks shift to lower energies and the peak at 250 cm^{-1} loses it relative intensity. When the sample is visibly heat damaged, a hematite (Fe_2O_3) [25] spectrum appears. Furthermore, EDS measurements in the damaged spot show a decrease in the amount of Se along with the appearance of oxygen, while outside the spot the amount of Se and Fe are stoichiometric.

In the lower panel of Fig. 5 the spectra polarization dependence is shown. The legend indicates the laser and analyzer polarization angles in that order. The results show that the peak attributed to Se vibrations (178 cm^{-1}) corresponds to A_{1g} symmetry, and the one attributed to Fe (193 cm^{-1}) to B_{1g} symmetry, in agreement with Gnezdilov *et al.* in Ref. [24]. The new peak observed at 250 cm^{-1} has the same polarization dependence as the one at 178 cm^{-1}.

B. Raman spectra temperature dependence

Temperature dependence of the Raman spectra taken on the sample from Fig. 2(b) are shown in Figs. 4 and 5. At room temperature, the two peaks of the cleaved part (Fig. 4) are at 179.8 and 193 cm^{-1}, whereas the new peak that appears for the aged part (Fig. 5) is at 250 cm^{-1}, along with the broad

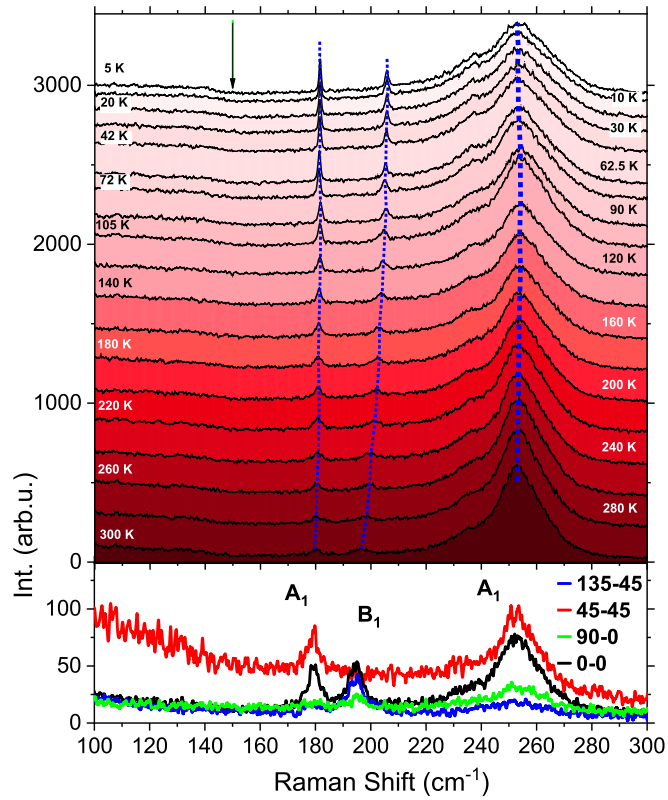

FIG. 5. Upper section: Raman measurements for the noncleaved part of the sample as a function of temperature below room temperature. The arrow indicates the beginning of the broad phonon tail below 150 cm^{-1}. In the lower section spectra polarization dependence is shown. The legend indicates the laser and analyzer polarization angle; on the top of each peak we display its normal mode representation.

phonon tail below 150 cm^{-1}. The peak positions observed in the cleaved part remain in the aged part. All measurements displayed in Figs. 4 and 5 were made in parallel polarization configuration. Below room temperature both peaks present in the cleaved part of the sample shift to higher energies (see upper panel of Fig. 4) as it has been reported before [24]. As to the new peak present in the aged part, we observed small changes in its energy toward higher energies as temperature drops down to 5 K, see upper panel in Fig. 5. A more detailed analysis on the peak position and areas is presented in Sec. III C.

Measurements in a furnace at high vacuum, and parallel polarization configuration, were performed on an aged sample and a freshly cleaved sample up to 473 and 773 K, respectively. On the cleaved sample we observe a pronounced shift of the mode attributed to Fe towards lower energies, as expected, and a smaller shift of the mode attributed to Se. Above ≈453 K the two peaks tend to merge (Fig. 4). After the measurements we recover the original spectrum at 293 K. For the noncleaved sample we can see in Fig. 6 how the new peak at 250 cm^{-1} gradually disappears irreversibly. When temperature reaches 473 K it disappears. This temperature is in good agreement with the one reported for thermal decapping of selenium coverage in Ref. [17]. However, once the sample is cooled down to room temperature, there are regions that are visually different showing two surface colors. *Zone 1*: a peak at 182 cm^{-1} and signs of a peak at 219 cm^{-1} are observed. *Zone 2*: a peak at 192 cm^{-1} appears (see inset of Fig. 6).

This indicates that some kind of material segregation occurs in the surface of the aged sample upon heating. The new spectra observed in zone 1, along with its formation temperature, are in good agreement with the one reported for $FeSe_2$ [26], while the zone 2 is consistent with iron oxide [27]. It is worth mentioning that the presence of iron oxide and selenium in excess was also detected at the surface of aged samples in our XPS measurements (see Sec. III D).

C. Analysis of the results

A detailed analysis of the peaks is shown in Fig. 7. The area of each peak, corrected by the phonon thermal population, along with their positions, are obtained for each temperature from a Lorentzian fit, see Appendix E.

The results for the Raman cross section of the peaks corresponding to A_{1g}(Se) and B_{1g}(Fe) in the cleaved and not cleaved parts of the sample [see Fig. 2(b)] below room temperature are shown in Figs. 7(a) and 7(b). Raman cross section of A_{1g} and B_{1g} modes present at the cleaved part of the sample increases as temperature decreases down to the structural transition (T_s), highlighted by a shadow light-gray zone ranging from 80 to 90 K, where they exhibit a maximum. Meanwhile, in the case of the aged sample, both peaks exhibit a distinctive feature as we approach T_s where a discontinuity of the Raman cross section occurs. This feature is more pronounced in the B_{1g} case.

For the new peak at 250 cm^{-1} and its shoulder at 233 cm^{-1}, the results below room temperature can be seen in Fig. 7(c). The shoulder has a monotonous increase with decreasing temperature, except around the nematic transition temperature, where an anomaly can be distinguished. The main peak, at 250 cm^{-1}, has a similar behavior to the other peaks in the noncleaved part of the sample, displaying a monotonous behavior down to near T_s, where a discontinuity in the Raman cross section is observed.

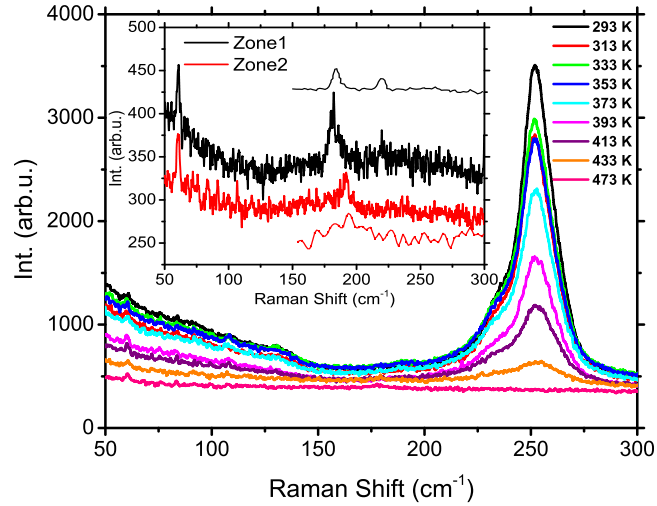

FIG. 6. Evolution of noncleaved sample spectrum from 293 to 473 K. Inset: Measurement at room temperature in two different positions of the sample after heating. The black line shows the spectra taken from the data of Ref. [26] for $FeSe_2$ and the dotted red line corresponds to an iron oxide (magnetite) Raman spectra [27].

The discontinuous change of the Raman cross section, observed below room temperature, of the modes A_{1g}, B_{1g}, and the new one at 250 cm^{-1} present in the aged parts of the sample, when approaching the nematic transition temperature indicates a strong correlation between electronic states and vibrational modes in this material. This suggests that the new peak near 250 cm^{-1} is intrinsic to the sample or belongs to a capping which is closely correlated to the bulk of the sample.

In Fig. 7(d) we show the Raman cross section from A_{1g} and B_{1g} peaks, in non-aged samples at all measured temperatures, ranging from 5 to 773 K. At T_s (also highlighted by a shadow gray zone ranging from 80 to 90 K) a maximum is observed. Above room temperature the Raman cross section of both peaks diminishes with increasing temperature up to 473 K, indicated by a dashed purple line, where they become indistinguishable (see Appendix E). Above this temperature, only one peak was fitted, labeled by "$A_{1g} + B_{1g}$." Pink circles were used to represent this convolved peak Raman cross section. In Fig. 7(d) the data below room temperature were vertically translated so they match with the measurements above room temperature.

In the case of the new peak observed in aged samples at 250 cm^{-1} and its shoulder, we see in Fig. 7(e) how above room temperature their Raman cross section diminish irreversibly up to 473 K, where it completely disappears, as previously mentioned.

From the fits we also determine each of the peaks energies, which are displayed for all the measured temperatures in Fig. 7(e). For the peak at 250 cm^{-1} and its shoulder, we observe a minimum in its energy-temperature dependence just above room temperature. This indicates that this aged part is not stable above room temperature. This is also supported by the resulting spectra after heating which indicates

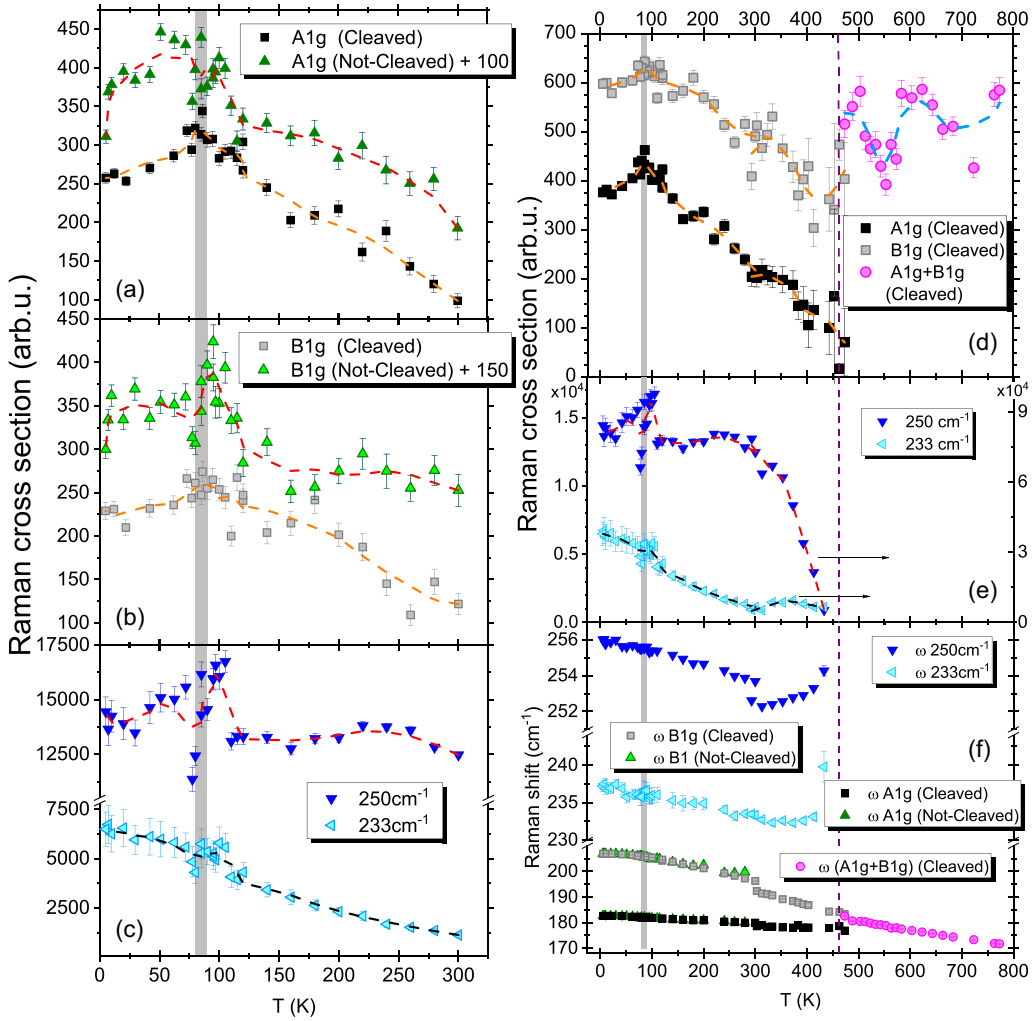

FIG. 7. Raman cross section versus temperature below room temperature for the cleaved and aged parts of the sample of modes (a) A_{1g}, (b) B_{1g}, and (c) 233 and 250 cm^{-1}. (d) Evolution of the Raman cross section of A_{1g} and B_{1g} modes for freshly cleaved samples is shown below and above room temperature. The data below room temperature were vertically translated to match the one above room temperature. Pink circles above 473 K (indicated by a dashed vertical purple line) correspond to the fit of the peak that results from the convolution of both modes. In (e) the Raman cross section temperature dependence of 233 and 250 cm^{-1} modes are shown. The left axis corresponds to the results below room temperature and the right axis to the ones above room temperature, indicated by arrows. Different samples were used in the low and high temperature runs. (f) The peaks energies as a function of temperature. The dashed lines on top of each data set corresponds to a 5 point average smooth. The shadow light gray in each graph indicates the structural transition temperature ranging from 80 to 90 K.

that material segregation occurs (see Sec. III B). Below room temperature the peak at 250 cm^{-1} has a linear energy shift towards higher energies, its rate of change diminishes below the structural and nematic transition temperature T_s.

As to the A_{1g} and B_{1g} energy dependence, we can see that below room temperature they have a linear energy shift towards higher energies, with the rate of change A_{1g} less pronounced than the one for B_{1g} (as was discussed in Ref. [24]). Both rates of change diminish below T_s, exhibiting the same behavior as the peak at 250 cm^{-1}. Besides, we observe that the energy dependence from the modes present both in the cleaved and aged part of the sample are identical.

Above room temperature, the energy-temperature dependence remains the same for both peaks while they tend to merge at about 473 K where they become indistinguishable, above this temperature we fit only one peak (see Appendix E). The rate of energy change of this convolved peak is slightly larger than the one calculated from the average of those of A_{1g} and B_{1g}. As can be seen in Fig. 7(d) and Appendix E, the A_{1g} Raman cross section has much less weight in the convolved peak than the B_{1g} one, thus a larger rate of energy change of the combined peak may be expected.

The energy dependence of all peaks except the one at 233 cm^{-1} has the same behavior below room temperature, exhibiting a change of slope below the structural transition. This fact supports the idea that the new peak at 250 cm^{-1} is intrinsic or belongs to a capping closely correlated to the bulk. This is not the case of the peak at 233 cm^{-1}, whose area and energy dependence are monotonous below room temperature. Above it, this peak is unstable. Although the two new peaks appear together, one is correlated to the bulk sample peaks, and the other one is not.

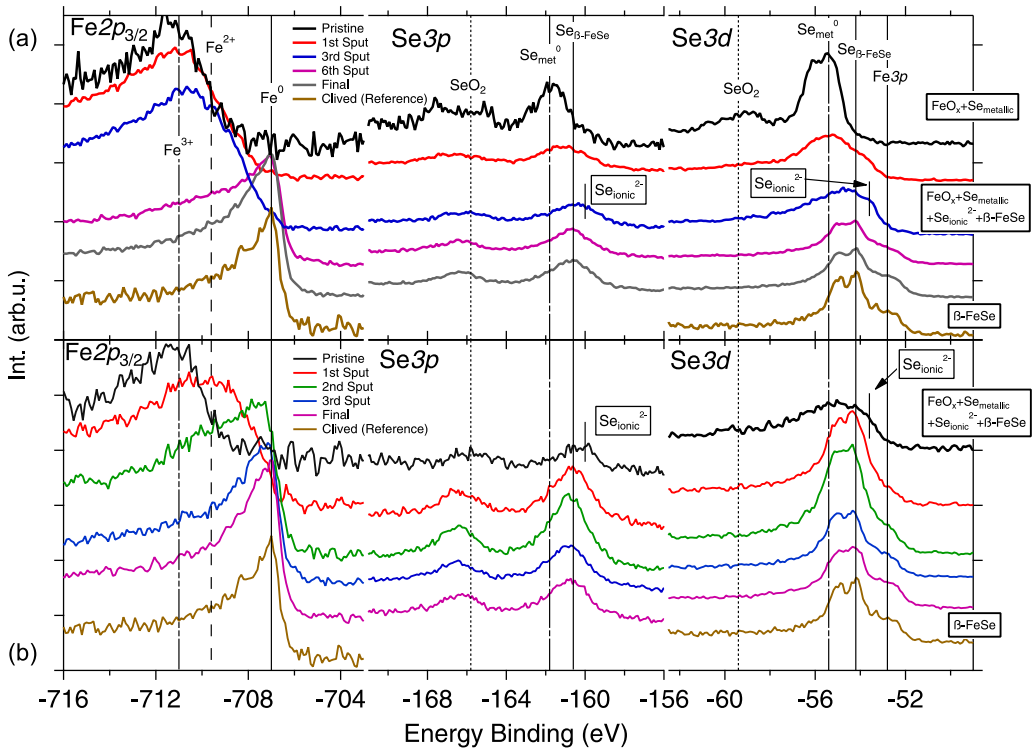

FIG. 8. Upper panel: Spectra taken at Fe_{2p}, Se_{3p}, and Se_{3d} energies, in an old sample surface **A**, which displays the mentioned Raman spectra (see Fig. 3 top panel) as a function of sputtering. Lower panel: Spectra taken from an old sample surface **B**, which does not display the new Raman feature as a function of sputtering. Brown curves in both panels correspond to spectra taken in a cleaved sample **C**. Vertical lines indicate the higher spin state binding energies for the different chemical species: FeO_x, Fe^0, Se^0, Se^{2-}, SeO_2, and β-FeSe. The boxes on the right indicate the composition on each stage of the sputtering depth profiling.

D. Surface chemical composition

An XPS study was conducted on β-FeSe crystal surfaces aged in air to have a better insight on the evolution with time of the surface chemical state of iron and selenium. We performed a depth profile study on β-FeSe surfaces aged in air for two months (**A**), one month (**B**), and on a just cleaved β-FeSe surface (**C**). **A** corresponds to an aged sample displaying the mentioned Raman feature while **B** and **C** display typical β-FeSe Raman spectra. The cleaved sample **C** was withdrawn from the high vacuum chamber after being measured with XPS and aged in air for a month (to become sample **B**).

The Fe 2p, Se 3p, and Se 3d spectra were analyzed, where the Se 3d partially overlaps with the Fe 3p core-level peak. In Fig. 8 the mentioned core-levels spectra on each sample surface are shown, with the intensity axes the same at each stage. The upper panel corresponds to the depth profile of sample **A**, and the lower panel to the depth profile of sample **B**. The brown curves on each panel correspond to the cleaved sample spectra **C** in the chemical state of pure β-FeSe compound, to which **A** and **B** converge.

For the cleaved surface **C** (after 15 min of sputtering with 2 kV) the main components of the Se 3d and Fe 2p core level were identified at BE = 54.2 eV and BE = 707 eV, both in close agreement with the reported values for the β-FeSe compound [28,29]. In the aged samples we performed a depth profiling with Ar^+ sputtering cycles at 2–3 kV over longer times. The estimated sputtering rate is 7 Å/min in the Ar^+ sputtering cycle at 2 kV. The total surface material removed is estimated around hundreds of nanometers in the case of sample **A** and tens of nanometers in the case of sample **B**.

The Fe chemical state is metallic on sample **C**, while is mainly oxidized in the other two aged samples (black curves). As we sputtered the surface the oxidized iron gradually disappears giving place to a metallic Fe signal (sharp peak at BE $\approx$ 707 eV). As this happens we observe how the chemical state of selenium, in both aged samples (**A** and **B**), is strongly modified.

In sample **A** we start with a surface mainly composed of iron oxide, metallic selenium (Se^0), and a small amount of SeO_2 [30] (only observed at this sample initial stage). After 5 min of sputtering at 2 kV, the pure metallic selenium is drastically reduced and completely disappeared after the third sputtering (blue curve in Fig. 8 upper panel). Also, at this point, the Se 3p peak shows contributions at lower BE than the one corresponding to the β-FeSe compound at BE $\approx$ 160 eV. A similar trend is observed in the Se 3d energy range, where a lower binding energy contribution appears at BE $\approx$ 53.6 eV (see labels Se^{2-} in the blue curve). From this point onwards there is a progressive appearance of the β-FeSe compound, as evidenced in the last two shown stages (pink and gray curves). There the Se 3p and Se 3d peaks show a main contribution at BE $\approx$ 160.6 eV and BE = 54.2 eV, respectively, and the Fe 2p and Fe 3p at BE = 707 eV and BE $\approx$ 52.8 eV, respectively.

For **B** sample (lower panel in Fig. 8) we observe that Se chemical state in the initial spectra (black curves) resemble the state of the **A** sample after the third sputtering (blue curve

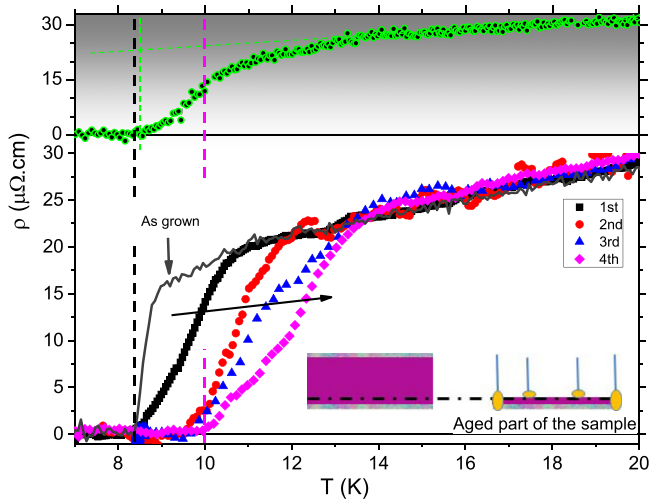

FIG. 9. Evolution of the superconducting onset temperature and critical temperature with thermal cycling in a sample with an aged surface. The dark gray line shows the resistivity versus temperature dependence of an *as-grown* sample. In the inset a scheme (not to scale) of the prepared sample is shown. Upper panel shows the transition region measured after one year in the same sample.

in Fig. 8 upper panel). At this stage we can clearly identify oxidized iron in the Fe $2p$ spectra. Also, in the Se $3p$ and Se $3d$ spectra there are contributions at lower BE than for the β-FeSe compound (see labels Se^{2-} in the black curve). As we continue to sputter, all the spectra resemble more and more the cleaved sample (**C**), reference spectra.

In the aged surface **B** we identify the contributions of Se^{-2} (see labels in the black curve, lower panel of Fig. 8) that becomes pure metallic Se^0 in the **A** surface, aged for longer times (black curve in Fig. 8 upper panel). This result suggests the formation of $Fe^{2+}Se^{2-}$ as an intermediate state, which decompose into FeO_x and bulk metallic Se^0. In conclusion, for surfaces aged longer in air, the β-FeSe compound decomposes into pure metallic Se that concentrate on top layers leaving the iron in oxidized states over many layers.

E. Electrical transport measurements

Taking into account the composition of the aged surface and being aware about the many reports on β-FeSe films and its critical transition temperature dependence with thickness [18,31,32], we proceed to measure the aged surface electrical transport properties. In the attempt to manipulate the aged surface as less as possible, we cleaved a sample and attached electrical contacts to this side, leaving on the other side an aged surface that was glued to a sapphire sample holder with a minimum amount of GE7031 varnish (see inset in Fig. 9).

In Fig. 9 we can observe that after a thermal cycling (up to 300 K) the sample onset and critical temperature (defined as zero resistivity temperature) rises. Besides, we have also observed small changes in the resistivity temperature dependence above the nematic transition. Initially $T_{\text{Onset}} = 10.5$ K and $T_c = 8.6$ K were measured. The final temperatures were $T_{\text{Onset}} = 13.8$ K and $T_c = 10$ K. This enhancement of T_c after thermal cycling was not observed in an as-grown (non-aged) sample, for which $T_{\text{Onset}} = 9$ K and $T_c = 8.4$ K. From our results, and using experimental data from Ref. [18] we estimate that a T_c of 10 K corresponds to a sample with an effective thickness of 80 nm (≈160 sheets) which is similar to the aged sample layer thickness measured by AFM (≈86 nm) and the removed thickness by sputtering in the case of sample **A**, see Sec. III D.

We remeasured the sample after one year, and the enhanced superconducting properties remain, as can be seen in the upper panel of Fig. 9. Nevertheless, no percolation at higher T_c is observed.

IV. DISCUSSION

There were conflicting conclusions regarding in which manner low dimensionality enhances the superconducting features in the case of β-FeSe films, and degrades them in the case of flakes taken from a single crystal of β-FeSe [33]. Also, it has been reported how the degradation of this material in air destroys the superconductivity [29]. There have been reports arguing the crucial role of stress in the appearance of superconductivity in films [34] as also in flakes [35].

We calculated the phonon dispersion relation using Bloch waves and group theory, considering a harmonic potential for one sheet of β-FeSe. The system formed by one sheet of β-FeSe corresponds to the C_{4v} point group, which has all of its A_1 and B_1 Raman modes active. The results of both methods are in good agreement, displaying three optical phonon modes with symmetries A_1, B_1, and A_1. The energy relationship of these modes was compared with our experimental results (A_{1g}, B_{1g}, and the new peak at 250 cm^{-1}) and the agreement between them is higher than 99%. Also the expected symmetries of the three vibrational modes correspond with the ones observed by polarization measurements: A_1 (180 cm^{-1}), B_1 (193 cm^{-1}), and A_1 (250 cm^{-1}); see lower panel in Fig. 5. For more information see Appendix A.

According to the XPS study performed in Sec. III D, we found evidence of the presence of a ionic compound, like $Fe^{+2}Se^{-2}$, as an intermediate state that decompose into FeO_x and bulk metallic Se^0. This result is in agreement with the work of Shesana *et al.* [30] that suggests the instability of this compound. As a result, the iron gets oxidized and the seleniums to which it was bond are released and begin to interact with each other, producing the observed a-Se Raman spectra present in the aged samples. As for the remaining β-FeSe present in the surface, it could result uncorrelated from the bulk in this mixed state producing a quasi-bidimensional behavior near the surface, originating a new Raman active peak, expected at ≈250 cm^{-1}. Another feature indicating the decorrelation of the aged surface is the appearance of a layer-breathing mode which comes along with the peak at 250 cm^{-1}, see Appendix B. This might explain the enhancement of the T_c assuming that the β-FeSe present in the aged part is not only uncorrelated from the bulk, but it is also stressed due to the differential contraction produced by the varnish which was used to attach the sample to a sapphire holder. The varnish contraction would also explain the dependence of T_c with the thermal cycling, since it could be producing a rearrangement of the surface material with higher percolation thresholds, improving the aged β-FeSe surface superconducting properties.

The peak at 250 cm^{-1} was also reported by Yang *et al.* in exfoliated sheets of β-FeSe crystals [23]. In this work they

report its appearance with aging, its relation to the sample thickness, and T_c degradation. They also assert that this new peak is due to the formation of amorphous selenium nanoparticles in the surface of the sample. According to Ref. [36] the peak at 250 cm^{-1} along with its shoulder corresponds to vibrational modes attributed to selenium allotropes of low dimensionality. Massat *et al.* [37], in the additional information, show the appearance of the new peak at 250 cm^{-1} along with the low energy feature below 150 cm^{-1}, in β-FeSe single crystals. In this work they report how the tail below 150 cm^{-1} is quenched due to the application of pressure along the c axis. We attribute the presence of this low energy tail to the Se acoustic branch which is observed as a step below the energy of its phonon gap [38] at 150 cm^{-1}. This is sustained in the loss of long-range translational symmetry (characteristic of amorphous materials), where the Raman selection rules for a crystalline material no longer hold. Also considering that the Raman signal at 250 cm^{-1} is only due to the formation of a-Se at the aged surface of the sample, we expect this to be depolarized. In this sense we performed a depolarization ratio analysis of this signal which unveil a polarized contribution to this new peak, see Appendix C.

The above discussed phenomena results in an old-surface coating, mainly composed of Se allotropes and iron oxide of ∼100 nm that protects the rest of the material. Cleavage is enough to remove this protective surface and recover the β-FeSe single crystal.

In order to see whether a similar aging process is also found in the layered, nonsuperconducting iron telluride β-FeTe compound, we have performed Raman measurements that are described in Appendix D. In this experiment the observed spectra on an aged sample is in good agreement with tellurium prepared in two-dimensional (2D) form. After cleaving the sample, we recover typical β-FeTe Raman spectra.

V. CONCLUSIONS

We propose that the changes in the Raman spectrum are due to the formation of $Fe^{2+}Se^{2-}$ (in ionic state) which, because of its instability, results in an oxidation of Fe atoms and free Se atoms in the surface of the sample. This layer acts as a cover capping, protecting the rest of the material. This could also produce a loss of translational symmetry from the remaining β-FeSe in the first aged sheets of the sample, near the surface, leading to a quasi-bidimensional (2D) behavior. According to our calculations, this originates a new Raman active mode at ≈250 cm^{-1}, which may be covered up by the presence of the a-Se spectra.

We correlate the T_c enhancement in transport experiments to the aged surface of the sample. The stress induced at the aged surface layer by either the chemical disordered interfaces or by the small amount of varnish, between sample and sample holder, is a plausible explanation for the increase in the critical temperature.

In the literature there are discrepancies about the origin of this new a-Se Raman peak at 250 cm^{-1} with its shoulder and with the low energy tail below 150 cm^{-1}. Also the presence of a similar phenomena observed in β-FeTe single crystals leads to the possibility that the aging process is ubiquitous to many binary chalcogenides compounds. A word of caution should be issued for future work in this kind of materials.

ACKNOWLEDGMENTS

We would like to acknowledge Armando A. Aligia and Nestor F. Haberkorn for their contributions to the discussion. M.L.A. acknowledges support from the Alexander von Humboldt Foundation. L.L., J.A.H., and G.N. acknowledge Agencia Nacional de Promoción Científica y Tecnológica (Grant No. PICT-2014-1265); CONICET (Grant No. PIP 2014-112 201301 00164co); Secretaría de Investigación, Internacionales y Postgrado Universidad Nacional de Cuyo (Grant No. 06/C018-T1) for financial support.

APPENDIX A: HARMONIC APPROXIMATION

The normal vibrational modes of one sheet of β-FeSe was modeled in the harmonic approximation. We consider our system as made by square unit cells (see pink dashed square in Fig. 10), within which there are four atoms: two Fe in the middle of the square faces, one Se above (or below) the iron plane in the center, and four atoms of Se below (or above) in the corners. This configuration corresponds to a C_{4v} symmetry group which has 12 Raman active modes, 3 A_1, 1 B_1, and 4 E. The modes with E representation are vibrations in x, y axes and the rest of them are vibrations along the z axis.

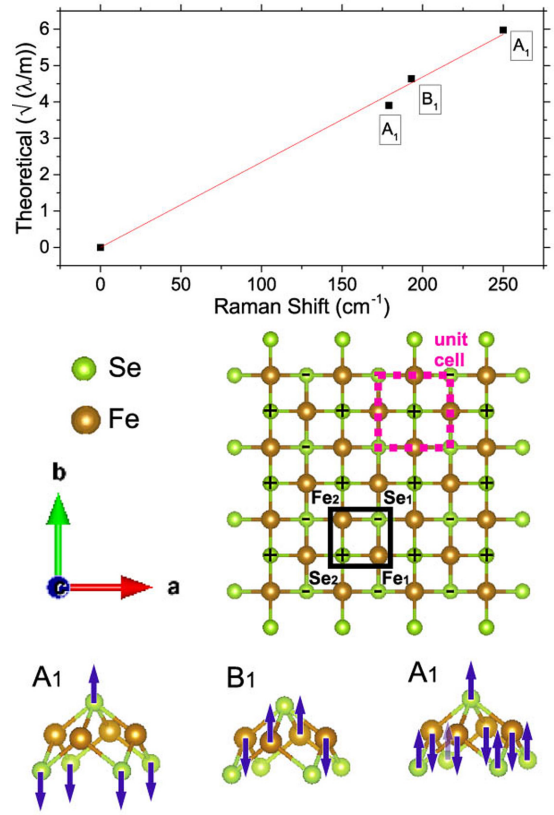

FIG. 10. Upper section: Fit of the experimental data with the theoretical calculations. λ is the eigenvalue from the theoretical calculation. Middle section: Scheme of one sheet of β-FeSe. The pink slashed line determines one arbitrary unit cell of the system and the black square shows the notation used for the Hamiltonian. Bottom section: Scheme of the vibrational modes along the c axis for a β-FeSe single sheet.

We consider interactions to second nearest neighbors, i.e., Se-Fe, Fe-Fe, and Se-Se interactions, as can be seen in the following Hamiltonian (see the black square in Fig. 10 as a guide for the index used for our calculation):

$$\begin{aligned}\mathcal{H} = \frac{K'}{2}\{&(Fe_{2y} - Se_{2y} + Se_{2z} - Fe_{2z})^2 \\ &+ (Fe_{1x} - Se_{2x} + Se_{2z} - Fe_{1z})^2 \\ &+ (Se_{1y} - Fe_{1y} + Fe_{1z} - Se_{1z})^2 \\ &+ (Se_{1x} - Fe_{2x} + Fe_{2z} - Se_{1z})^2\} \\ &+ \frac{C}{4}(Se_{1x} - Se_{2x} + Se_{1y} \\ &- Se_{2y} + Se_{2z} - Se_{1z})^2 \\ &+ \frac{D}{4}(Fe_{1x} - Fe_{2x} + Fe_{2y} - Fe_{1y})^2.\end{aligned}$$

This model predicts three optical modes in the center of the Brillouin zone. From lowest to highest energy: vibrations of Se atoms only, vibrations of Fe atoms only, and a combination of vibration of both kinds of atoms (see lower section of Fig. 10 for a scheme of each mode). The expected polarization symmetries of each mode are A_1 for the Se, B_1 for the Fe, and A_1 for the last mode. As mentioned in the general sample characterization section, the polarization dependence of the peaks is the same as the expected from our model. We compare the theoretical relative energy expected vs the experimental energy results, and the coefficient of determination (R^2) is higher than 0.99 for all temperatures. Also from the slope of the linear fit in Fig. 10 we estimated the bond energy (only taking into account first neighbor interactions, i.e., $K' \gg C$) of the covalent union of Fe-Se atoms obtaining a value of $\approx$1.5 eV.

APPENDIX B: LOW FREQUENCY LAYER-BREATHING MODE

Layered materials, whose atoms are linked by covalent bonds within a layer (intralayer) and have an interlayer interaction of van der Waals nature, have characteristic vibrational modes in the low frequency Raman spectra. These are known as the breathing mode and the shearing mode, which correspond to vibrations between layers along the direction normal to the plane and in-plane displacement, respectively. In particular, the frequency of these modes could be used to describe and characterize the interlayer coupling and the number of layers involved in the mode [39].

In our experiment we have observed that these modes appear with aging. We measured a sample displaying typical β-FeSe spectrum, and two months later we observed how the new peak at 250 cm^{-1} appears, along with a peak at low energy at $\sim$82 cm^{-1}, with satellites on each side, see Fig. 11.

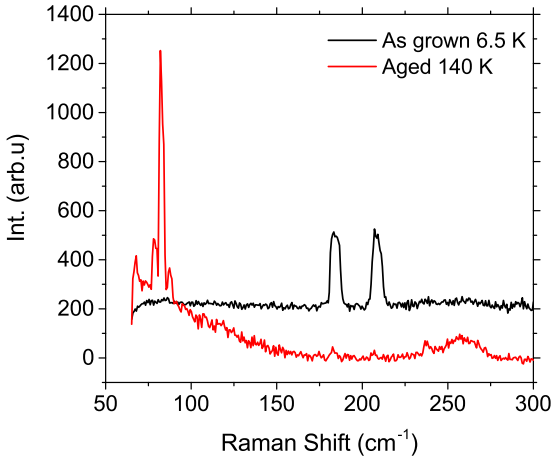

FIG. 11. Black curve: Typical β-FeSe spectrum taken at 6.5 K. Red curve: Spectrum from the same sample 2 months later at 140 K. We see how the layer-breathing mode appears along with the new peak at 250 cm^{-1}. Black curve was vertically translated for clarity.

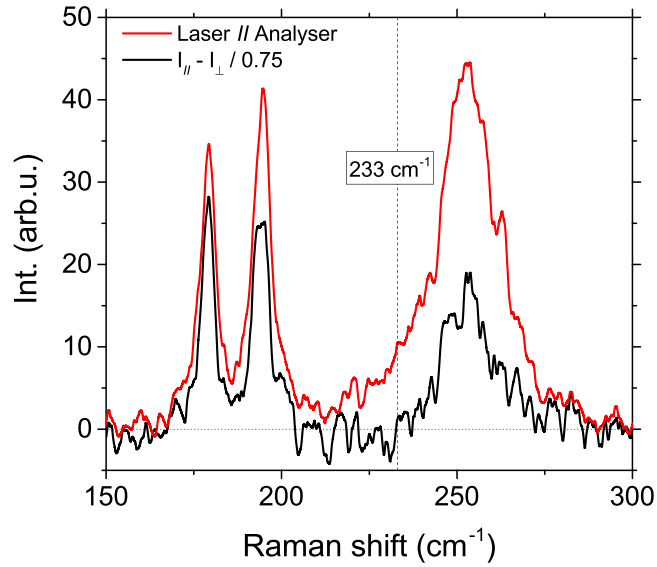

FIG. 12. Red curve: Spectrum collected with laser and analyzer polarization parallel to each other at 300 K. Black curve: Same spectrum after depolarization ratio analysis. We observe how the peak at 233 cm^{-1} completely disappears.

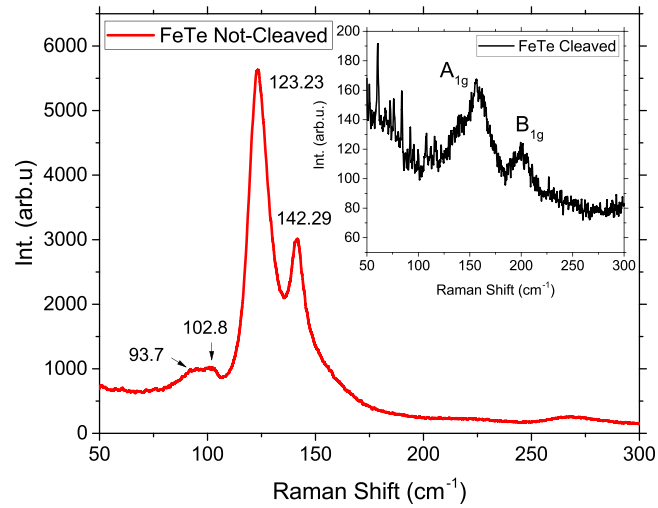

FIG. 13. Raman spectra of FeTe single crystal before and after cleaving at room temperature. The peak values in the main frame are obtained fitting Lorentzian shaped curves.

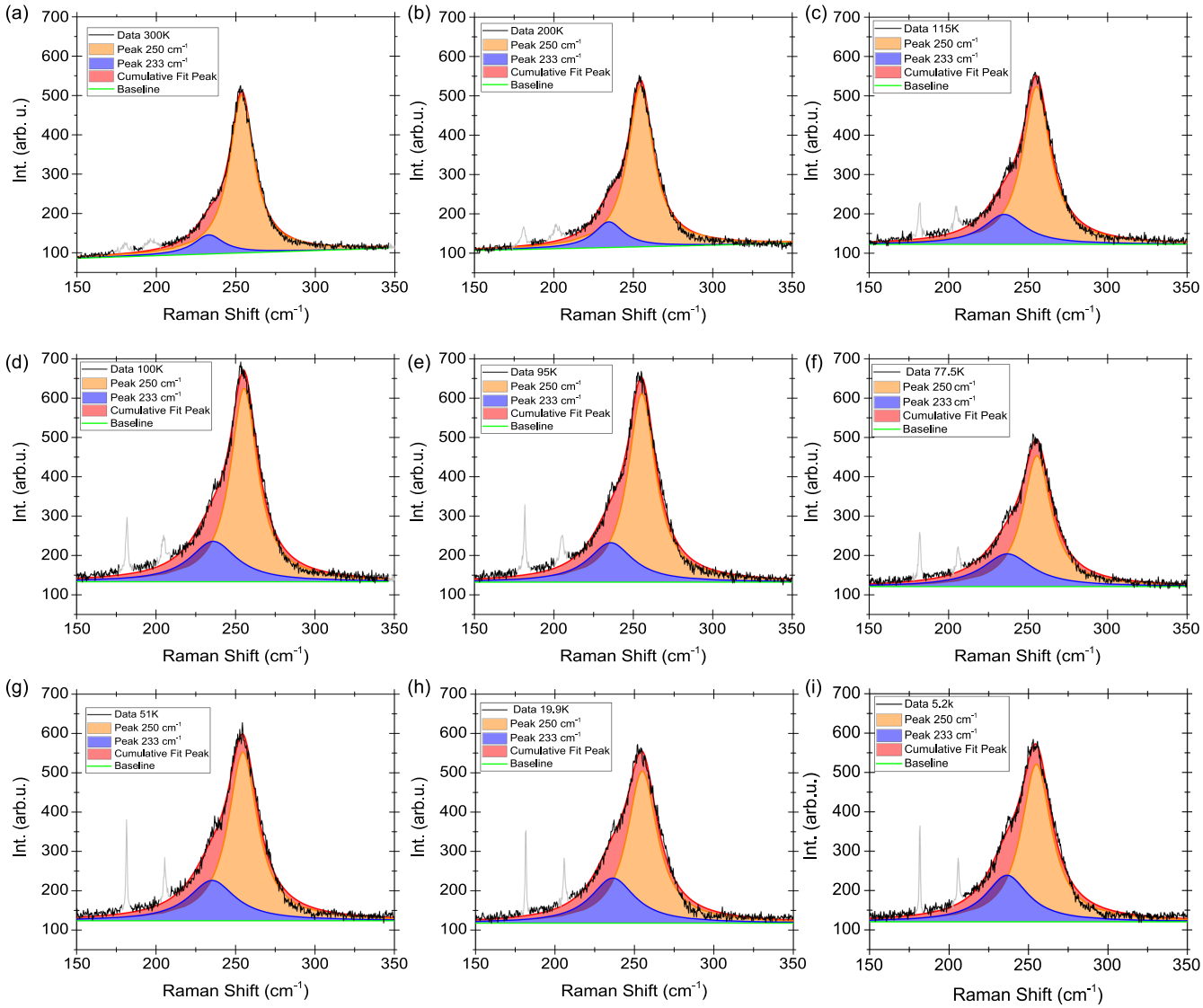

FIG. 14. Experimental spectra of the 250 and 233 cm^{-1} peaks and their fits taken at (a) 300 K, (b) 200 K, (c) 115 K, (d) 100 K, (e) 95 K, (f) 77.5 K, (g) 51 K, (h) 19.9 K, and (i) 5.2 K. The light gray line shows A_{1g} and B_{1g} peaks which were subtracted to perform the fit.

The measurements shown in Fig. 11 were made in a macro backscattering configuration with a 514 nm wavelength laser.

A simple one-dimensional model described in Ref. [39] by Liang *et al.*, where each layer is considered as a body whose neighbors are along the c axis, gives these vibrational mode energies as a function of the number of layers, the unit cell density mass, and the van der Waals force constant. The calculated value of the force constant in our experiment is consistent with the ones reported for similar systems.

APPENDIX C: DEPOLARIZATION RATIO ANALYSIS

Assuming that the new signal observed in aged samples, i.e., the new peak at 250 cm^{-1} with its shoulder at 233 cm^{-1} and the tail below 150 cm^{-1}, is due to the presence of amorphous selenium (a-Se) at the surface, this signal should be depolarized since a-Se has no crystalline order. In this sense we performed a depolarization ratio analysis [40,41] of the spectra presented in Fig. 5 lower panel. The depolarization ratio is defined as the ratio of the Raman intensity collected when the polarization of incident and scattered light are perpendicular to that collected when the polarization of incident and scattered light are parallel to each other, $\rho = I_{\perp}/I_{\parallel}$. According to Placzek's polarizability approximation, this ratio is less than 0.75 for totally symmetric vibrational mode (polarized), and equal to or grater than 0.75 for the others (depolarized) [41]. So we can say

$$0 < I_{\parallel} - I_{\perp}/0.75 \rightarrow \text{Polarized mode},$$
$$0 \geqslant I_{\parallel} - I_{\perp}/0.75 \rightarrow \text{Depolarized mode}. \qquad \text{(C1)}$$

In Fig. 12 we can see a spectrum where the polarization of the incident laser beam and analyzer are parallel (red curve) and a spectrum where the depolarization ratio analysis from Eq. (C1) was performed (black curve). From the analysis we see that the peak at 250 cm^{-1} has a polarized component. We attribute this polarized component to the new mode predicted

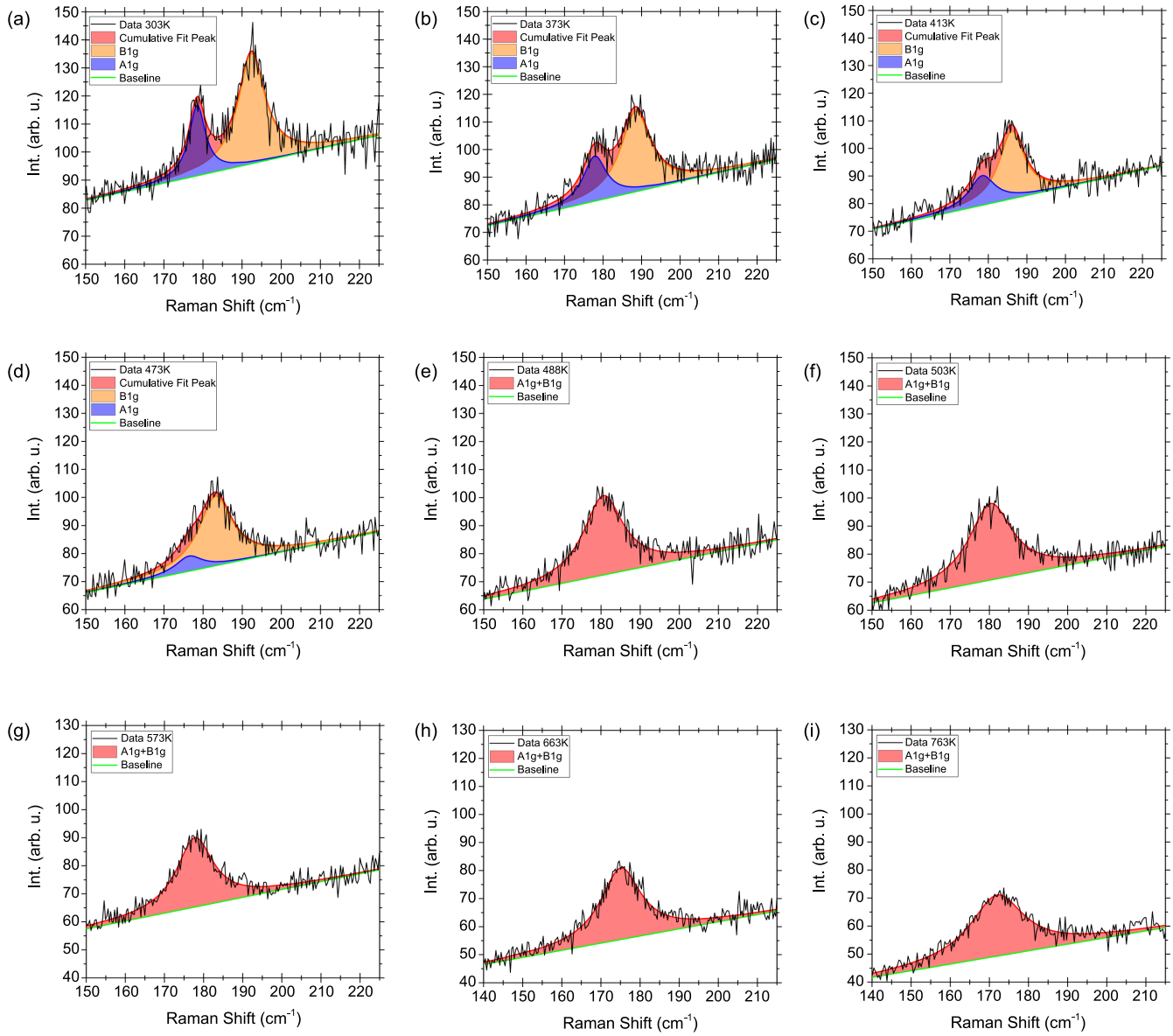

FIG. 15. Measured A_{1g} and B_{1g} peaks and their fits taken at (a) 303 K, (b) 373 K, (c) 413 K, (d) 473 K, (e) 488 K, (f) 503 K, (g) 573 K, (h) 663 K, and (i) 763 K.

by the model from Appendix A since crystalline selenium signal should be found at 233 cm^{-1} [42].

APPENDIX D: RELATED RESULTS AND MATERIALS

In order to search for the appearance of 2D behavior with aging in a related material, we have measured the Raman spectra at room temperature for a β-FeTe single crystalline sample [43] aged in air, before and after cleaving. The spectra are shown in Fig. 13 displaying very different sets of peaks. The measurements before cleavage display peaks at: 93.7(3), 102.8(3), 123.23(2), 142.29(6) cm^{-1}, and overtones. This spectrum features correspond to those found in elemental tellurium prepared in a 2D form [44]. After cleaving, the measurement shows two peaks at 157 and 200 cm^{-1} consistent with the Raman spectra of single crystal β-FeTe [45].

APPENDIX E: DECONVOLUTION AND FITS

For the data analysis from Sec. III C we deconvolve the peak observed at aged samples in two peaks by Lorentzian fits, one at 250 cm^{-1} and other at 233 cm^{-1}. The contribution of A_{1g} and B_{1g} was subtracted from the data. Some fits can be seen in Fig. 14. The coefficient of determination is $R^2 \approx 0.99$ for all temperatures.

In Fig. 15 we display the high temperature measurements of the A_{1g} and B_{1g} peaks and its fits. As temperature rises, both peaks shift towards lower energies with different rates (see Fig. 7) up to 473 K; beyond this temperature, both peaks become indistinguishable within the error.

All the analyzed data were corrected by the phonon thermal population, this is performed by dividing the peak's intensity by $(n + 1)$, where n is the the Bose factor for the corresponding temperature.

[1] J. P. Sun, K. Matsuura, G. Z. Ye, Y. Mizukami, M. Shimozawa, K. Matsubayashi, M. Yamashita, T. Watashige, S. Kasahara, Y. Matsuda, J.-Q. Yan, B. C. Sales, Y. Uwatoko, J.-G. Cheng, and T. Shibauchi, Dome-shaped magnetic order competing with high-temperature superconductivity at high pressures in FeSe, Nat. Commun. **7**, 12146 (2016).

[2] T. M. McQueen, Q. Huang, V. Ksenofontov, C. Felser, Q. Xu, H. Zandbergen, Y. S. Hor, J. Allred, A. J. Williams, D. Qu, J. Checkelsky, N. P. Ong, and R. J. Cava, Extreme sensitivity of superconductivity to stoichiometry in $Fe_{1+\delta}Se$, Phys. Rev. B **79**, 014522 (2009).

[3] A. E. Böhmer, F. Hardy, F. Eilers, D. Ernst, P. Adelmann, P. Schweiss, T. Wolf, and C. Meingast, Lack of coupling between superconductivity and orthorhombic distortion in stoichiometric single-crystalline FeSe, Phys. Rev. B **87**, 180505(R) (2013).

[4] K. Zakeri, T. Engelhardt, T. Wolf, and M. Le Tacon, Phonon dispersion relation of single-crystalline β-FeSe, Phys. Rev. B **96**, 094531 (2017).

[5] H. K. Vivanco and E. E. Rodriguez, The intercalation chemistry of layered iron chalcogenide superconductors, J. Solid State Chem. **242**, 3 (2016).

[6] D. L. Duong, S. J. Yun, and Y. H. Lee, van der Waals layered materials: Opportunities and challenges, ACS Nano **11**, 11803 (2017).

[7] P. Zhang, K. Yaji, T. Hashimoto, Y. Ota, T. Kondo, K. Okazaki, Z. Wang, J. Wen, G. D. Gu, H. Ding, and S. Shin, Observation of topological superconductivity on the surface of an iron-based superconductor, Science **360**, 182 (2018).

[8] D. Wang, L. Kong, P. Fan, H. Chen, S. Zhu, W. Liu, L. Cao, Y. Sun, S. Du, J. Schneeloch, R. Zhong, G. Gu, L. Fu, H. Ding, and H.-J. Gao, Evidence for Majorana bound states in an iron-based superconductor, Science **362**, 333 (2018).

[9] L. Lauke, R. Heid, M. Merz, T. Wolf, A.-A. Haghighirad, and J. Schmalian, Band engineering of Dirac cones in iron chalcogenides, Phys. Rev. B **102**, 054209 (2020).

[10] Y. D. Glinka, S. Babakiray, T. A. Johnson, and D. Lederman, Thickness tunable quantum interference between surface phonon and Dirac plasmon states in thin films of the topological insulator Bi_2Se_3, J. Phys.: Condens. Matter **27**, 052203 (2015).

[11] H.-H. Kung, M. Salehi, I. Boulares, A. F. Kemper, N. Koirala, M. Brahlek, P. Lošťák, C. Uher, R. Merlin, X. Wang, S.-W. Cheong, S. Oh, and G. Blumberg, Surface vibrational modes of the topological insulator Bi_2Se_3 observed by Raman spectroscopy, Phys. Rev. B **95**, 245406 (2017).

[12] Y. Li, M. Han, Z. Zhou, X. Xia, Q. Chen, and M. Chen, Topological insulator-assisted $MoSe_2/Bi_2Se_3$ heterostructure: Achieving fast reaction kinetics toward high rate sodium-ion batteries, ChemElectroChem **8**, 697 (2021).

[13] D. Nam, J.-U. Lee, and H. Cheong, Excitation energy dependent Raman spectrum of $MoSe_2$, Sci. Rep. **5**, 17113 (2015).

[14] D. B. Lioi, D. J. Gosztola, G. P. Wiederrecht, and G. Karapetrov, Photon-induced selenium migration in $TiSe_2$, Appl. Phys. Lett. **110**, 081901 (2017).

[15] P. Goli, J. Khan, D. Wickramaratne, R. K. Lake, and A. A. Balandin, Charge density waves in exfoliated films of van der Waals materials: Evolution of Raman spectrum in $TiSe_2$, Nano Lett. **12**, 5941 (2012).

[16] S. J. Cartamil-Bueno, P. G. Steeneken, F. D. Tichelaar, E. Navarro-Moratalla, W. J. Venstra, R. van Leeuwen, E. Coronado, H. S. J. van der Zant, G. A. Steele, and A. Castellanos-Gomez, High-quality-factor tantalum oxide nanomechanical resonators by laser oxidation of $TaSe_2$, Nano Res. **8**, 2842 (2015).

[17] J. Dai, W. Wang, M. Brahlek, N. Koirala, M. Salehi, S. Oh, and W. Wu, Restoring pristine Bi_2Se_3 surfaces with an effective Se decapping process, Nano Res. **8**, 1222 (2015).

[18] Q. Wang, W. Zhang, Z. Zhang, Y. Sun, Y. Xing, Y. Wang, L. Wang, X. Ma, Q.-K. Xue, and J. Wang, Thickness dependence of superconductivity and superconductor-insulator transition in ultrathin FeSe films on $SrTiO_3(001)$ substrate, 2D Mater. **2**, 044012 (2015).

[19] P. Carroll and J. Lannin, Inelastic light scattering from liquid and amorphous selenium, J. Non-Cryst. Solids **35-36**, 1277 (1980).

[20] P. Carroll and J. Lannin, Raman scattering of amorphous selenium films, Solid State Commun. **40**, 81 (1981).

[21] M. L. Amigó, M. V. Ale Crivillero, D. G. Franco, J. Guimpel, and G. Nieva, Influence of the Fe concentration on the superconducting properties of $Fe_{1-y}Se$, J. Low Temp. Phys. **179**, 15 (2015).

[22] T. Mousavi, C. Grovenor, and S. Speller, Structural parameters affecting superconductivity in iron chalcogenides: A review, Mater. Sci. Technol. **30**, 1929 (2014).

[23] R. Yang, W. Luo, S. Chi, D. Bonn, and G. M. Xia, The stability of exfolicated FeSe nanosheets during in-air device fabrication processes, IEEE Trans. Nanotechnol. **18**, 37 (2019).

[24] V. Gnezdilov, Y. G. Pashkevich, P. Lemmens, D. Wulferding, T. Shevtsova, A. Gusev, D. Chareev, and A. Vasiliev, Interplay between lattice and spin states degree of freedom in the FeSe superconductor: Dynamic spin state instabilities, Phys. Rev. B **87**, 144508 (2013).

[25] J. C. Bridges, M. J. Burchell, H. C. Changela, N. J. Foster, J. A. Creighton, J. D. Carpenter, S. J. Gurman, I. A. Franchi, and H. Busemann, Iron oxides in comet 81P/Wild 2, Meteoritics & Planetary Sci. **45**, 55 (2010).

[26] B. Yuan, X. Hou, Y. Han, W. Luan, and S.-t. Tu, Facile synthesis of flake-like $FeSe_2$ particles in open-air conditions, New J. Chem. **36**, 2101 (2012).

[27] O. N. Shebanova and P. Lazor, Raman spectroscopic study of magnetite ($FeFe_2O_4$): A new assignment for the vibrational spectrum, J. Solid State Chem. **174**, 424 (2003).

[28] A. Yamasaki, Y. Matsui, S. Imada, K. Takase, H. Azuma, T. Muro, Y. Kato, A. Higashiya, A. Sekiyama, S. Suga, M. Yabashi, K. Tamasaku, T. Ishikawa, K. Terashima, H. Kobori, A. Sugimura, N. Umeyama, H. Sato, Y. Hara, N. Miyagawa *et al.*, Electron correlation in the FeSe superconductor studied by bulk-sensitive photoemission spectroscopy, Phys. Rev. B **82**, 184511 (2010).

[29] D. Telesca, Y. Nie, J. I. Budnick, B. O. Wells, and B. Sinkovic, Impact of valence states on the superconductivity of iron telluride and iron selenide films with incorporated oxygen, Phys. Rev. B **85**, 214517 (2012).

[30] M. Shenasa, S. Sainkar, and D. Lichtman, XPS study of some selected selenium compounds, J. Electron Spectrosc. Relat. Phenom. **40**, 329 (1986).

[31] Q.-Y. Wang, Z. Li, W.-H. Zhang, Z.-C. Zhang, J.-S. Zhang, W. Li, H. Ding, Y.-B. Ou, P. Deng, K. Chang, J. Wen, C.-L. Song, K. He, J.-F. Jia, S.-H. Ji, Y.-Y. Wang,

L.-L. Wang, X. Chen, X.-C. Ma, and Q.-K. Xue, Interface-induced high-temperature superconductivity in single unit-cell FeSe films on $SrTiO_3$, Chin. Phys. Lett. **29**, 037402 (2012).

[32] D. Liu, W. Zhang, D. Mou, J. He, Y.-B. Ou, Q.-Y. Wang, Z. Li, L. Wang, L. Zhao, S. He *et al.*, Electronic origin of high-temperature superconductivity in single-layer FeSe superconductor, Nat. Commun. **3**, 931 (2012).

[33] L. Farrar, M. Bristow, A.-A. Haghighirad, A. McCollam, S. Bending, and A. Coldea, Suppression of superconductivity and enhanced critical field anisotropy in thin flakes of fese, npj Quantum Mater. **5**, 29 (2020).

[34] F. Nabeshima, Y. Imai, M. Hanawa, I. Tsukada, and A. Maeda, Enhancement of the superconducting transition temperature in FeSe epitaxial thin films by anisotropic compression, Appl. Phys. Lett. **103**, 172602 (2013).

[35] X. Wang, Z. Zhang, W. Wang, Y. Zhou, X. Kan, X. Chen, C. Gu, L. Zhang, L. Pi, Z. Yang, and Y. Zhang, Enhancement of superconductivity in FeSe thin crystals induced by biaxial compressive strain, Physica C **537**, 1 (2017).

[36] A. H. Goldan, C. Li, S. J. Pennycook, J. Schneider, A. Blom, and W. Zhao, Molecular structure of vapor-deposited amorphous selenium, J. Appl. Phys. **120**, 135101 (2016).

[37] P. Massat, Y. Quan, R. Grasset, M.-A. Méasson, M. Cazayous, A. Sacuto, S. Karlsson, P. Strobel, P. Toulemonde, Z. Yin, and Y. Gallais, Collapse of Critical Nematic Fluctuations in FeSe under Pressure, Phys. Rev. Lett. **121**, 077001 (2018).

[38] F. Y. Hansen, G. P. Alldredge, and H. L. McMurry, Calculation of the phonon density of states and related thermodynamic properties for trigonal selenium, J. Chem. Phys. **78**, 921 (1983).

[39] L. Liang, J. Zhang, B. G. Sumpter, Q.-H. Tan, P.-H. Tan, and V. Meunier, Low-frequency shear and layer-breathing modes in raman scattering of two-dimensional materials, ACS Nano **11**, 11777 (2017).

[40] C. D. Allemand, Depolarization ratio measurements in Raman spectrometry, Appl. Spectrosc. **24**, 348 (1970).

[41] C. N. Banwell and E. M. McCash, *Fundamentals of Molecular Spectroscopy* (McGraw-Hill, Berkshire, England, 1994).

[42] S. Peng, G. Tang, K. Huang, Q. Qian, D. Chen, Q. Zhang, and Z. Yang, Crystalline selenium core optical fibers with low optical loss, Opt. Mater. Express **7**, 1804 (2017).

[43] M. V. Ale Crivillero, Influence of the crystalline structure and the mesostructure on the physical properties β-FeSe based thin films and heterostructures, Ph.D. thesis, Instituto Balseiro, UNCuyo, 2019, https://ricabib.cab.cnea.gov.ar/864/.

[44] S. Khatun, A. Banerjee, and A. J. Pal, Nonlayered tellurene as an elemental 2D topological insulator: Experimental evidence from scanning tunneling spectroscopy, Nanoscale **11**, 3591 (2019).

[45] T.-L. Xia, D. Hou, S. C. Zhao, A. M. Zhang, G. F. Chen, J. L. Luo, N. L. Wang, J. H. Wei, Z.-Y. Lu, and Q. M. Zhang, Raman phonons of α-FeTe and $Fe_{1.03}Se_{0.3}Te_{0.7}$ single crystals, Phys. Rev. B **79**, 140510(R) (2009).